Journal of ELECTRONIC MATERIALS
DOI: 10.1007/s11664-013-2898-z

Power Factor Enhancement by Inhomogeneous Distribution of Dopants in Two-Phase Nanocrystalline Systems

NEOPHYTOS NEOPHYTOU,[1,2] XANTHIPPI ZIANNI,[3,4,9] HANS KOSINA,[1] STEFANO FRABBONI,[5,6] BRUNO LORENZI,[7] and DARIO NARDUCCI[7,8]

1.—Institute for Microelectronics, Technical University of Vienna, 1040 Vienna, Austria. 2.—School of Engineering, University of Warwick, Coventry CV4 7AL, UK. 3.—Department of Aircraft Technology, Technological Educational Institution of Sterea Ellada, 34 400 Psachna, Greece. 4.—Department of Microelectronics, IAMPPNM, NCSR 'Demokritos', 153 10 Athens, Greece. 5.—Department of Physics, Computer Science and Mathematics, University of Modena and Reggio Emilia, Via G. Campi 213/A, 41125 Modena, Italy. 6.—CNR-Institute of Nanoscience-S3, Via G. Campi 213/A, 41125 Modena, Italy. 7.—Department of Materials Science, University of Milano Bicocca, Via R. Cozzi 53, 20125 Milan, Italy. 8.—Consorzio DeltaTi Research, Milan, Italy. 9.—e-mail: xzianni@gmail.com

In this work, we describe a novel idea that allows for high thermoelectric power factors in two-phase materials that are heavily doped with an inhomogeneous distribution of dopants. We show that a concurrent increase of the electrical conductivity and Seebeck coefficient and a consequent increase of the power factor can be achieved in such systems. To explain the concept, we employ a semiclassical one-dimensional model that considers both electron and phonon transport through a series connection of two-phases of the material. We discuss microscopic characteristics of the material and the formation of the two phases (grains and grain boundaries in our case) by the inhomogeneous distribution of dopants in the polycrystalline material. Our theoretical investigation reveals that: (1) the improvement in the Seebeck coefficient can be attributed to carrier filtering due to the energy barriers at the grain boundaries, and to the difference in the lattice thermal conductivity of the grains and grain boundaries, and (2) the improvement in the electrical conductivity is a result of a high Fermi level in the grains. This allows high energy carriers to contribute to transport, which increases the impurity scattering limited mean-free-path, and increases the conductivity in the grains and thus in the whole material. Such an unexpected concurrent increase of the electrical conductivity and the Seebeck coefficient was recently observed in heavily boron-doped polycrystalline silicon of grain sizes < 100 nm in which a silicon-boride phase is formed around the grain boundaries. We provide a simple 1D model that explains the behavior of this system, indicating processes that can take place in heavily doped nanocrystalline materials.

Key words: Thermoelectric transport properties, thermoelectric power factor, barrier, nanocrystalline, model

INTRODUCTION

The use of nanostructures has been established as the most promising approach in improving thermoelectric efficiency.[1–5] The thermoelectric performance

(Received July 12, 2013; accepted October 29, 2013)

Published online: 26 November 2013

of a material is quantified by the dimensionless figure of merit $ZT = \sigma S^2 T/\kappa$, where σ is the electrical conductivity, S is the Seebeck coefficient, and κ is the thermal conductivity. Traditionally, ZT remained low (below 1 for most bulk materials) because of the adverse interdependence of the electrical conductivity and the Seebeck coefficient and high thermal conductivities. In recent years, however, much larger ZT values have been achieved in nanostructures due to a significant reduction in their thermal conductivity.[6,7] This was achieved even for traditionally poor thermoelectric materials such as Si. The room temperature ZT in Si nanowires and nanomeshes, for example, was reported to increase to $ZT \sim 0.5$ from $ZT \sim 0.01$, due to an almost two orders of magnitude reduction in thermal conductivity.[8–10] However, no progress has yet been reported on the use of nanostructuring in improving the power factor σS^2.[11,12] Recent experimental work has reported large Seebeck coefficients in a variety of nanostructured materials such as MnO_2 powders,[13] PbTe nanowires,[14] oxide nanofibers,[15] two-dimensional $SrTiO_3$ electron gas channels,[16] heavily-doped Si,[17] materials with impurity resonant levels,[18] and superlattices,[19] but the thermoelectric power factor has still been limited due to the severe degradation of the electrical conductivity in these structures.

In a very recent work, however, we demonstrated that a large power factor enhancement can be achieved in nanocrystalline Si under extremely high boron doping concentrations.[1–5] This is due to the fact that, for a range of carrier concentration, the Seebeck coefficient and the electrical conductivity increased *simultaneously*. In that case, the geometry was rather complicated, consisting of a 3D network of grains and grain boundaries. The grains were on average 30 nm in diameter, whereas the grain boundaries had a thickness of 2 nm. What is important in that geometry, however, is that the size of the average grain is such that the carrier momentum is completely relaxed, whereas the carrier energy is only partially relaxed. In this work, we demonstrate the principle which leads to the large power factors. In our model approach, we simplify the geometry assuming a 1D network of alternating grains (wells) and grain boundaries (barriers), and focus on the parameter values required to achieve such high power factors. Although a detailed description of real structures such as this presented in Refs. 1–5 may require a more sophisticated 3D description, the physics behind these experimental findings is adequately captured by our 1D model. We present a semiclassical model that explains the observed behavior by considering both electron and phonon transport. It focuses on the microscopic characteristics of the material, and particularly on the inhomogeneous distribution of the boron dopants in the grains and the grain boundaries, which gives rise to the effect we describe. It can be anticipated that the inhomogeneous impurity distribution evolves after sequential annealing steps to the final form that allows for high conductivity in the grains and high Seebeck coefficient in the grain boundaries of the material. The paper is organized as follows: In Section II, we describe the transport model. In Section III, we discuss the potential profile that arises from the inhomogeneous distribution of dopants in the two-phase material. Section IV presents the thermoelectric coefficient calculations for the 1D model system, and compares with the measured data for the nano-crystalline material. Finally, Section V summarizes and concludes the work.

TRANSPORT MODEL

Transport Model for the Bulk Material

We employ the linearized Boltzmann theory, within which the electrical conductivity and the Seebeck coefficient are given by the following expressions:[20,21]

$$\sigma = q_0^2 \int_{E_0}^{\infty} dE \left(-\frac{\partial f_0}{\partial E}\right) \Xi(E), \tag{1a}$$

$$S = \frac{q_0 k_B}{\sigma} \int_{E_0}^{\infty} dE \left(-\frac{\partial f_0}{\partial E}\right) \Xi(E) \left(\frac{E - E_F}{k_B T}\right), \tag{1b}$$

where the transport distribution function $\Xi(E)$is defined as:[20,21]

$$\Xi(E) = N(E)\upsilon(E)\lambda(E), \tag{2}$$

where $\upsilon(E)$ is the bandstructure velocity, $N(E)$ is the density of states (DOS), and $\lambda(E)$ is the mean-free-path (MFP) for scattering. The overall MFP includes all relevant scattering mechanisms and is computed using Matthiessen's rule. In this work, we include phonon scattering and ionized impurity scattering. In Eq. 2, a simple way to describe the energy dependence of the MFP for a specific scattering mechanism, i, is through a power law with a characteristic exponent r as $\lambda_i(E/k_B T)^r$. λ_i is the MFP, and the exponent r depends on the scattering mechanism and the dimensionality of the problem. In the case of phonon scattering in the 3D material, we consider, for example, that the MFP for phonons is energy-independent ($r = 0$),[22,23] and consequently the scattering rate is proportional to the DOS.

In the calculations, we include phonon and ionized impurity scattering. For ionized impurity scattering, which limits transport in our reference highly doped material, different expressions for the scattering rate and for the screening length work better for different doping concentrations.[23–25] We use the Brooks–Herring model as described in Ref. 23, in which the momentum relaxation time is given by:

$$\tau(E) = \frac{16\pi\varepsilon_{Si}^2\sqrt{2m_{DOS}}}{q_0^4 N_I}\left(\ln(1+\gamma^2) - \frac{\gamma^2}{1+\gamma^2}\right)^{-1} \times (E-E_0)^{3/2}, \quad (3a)$$

where

$$\gamma^2 = \frac{8m_{DOS}(E-E_0)L_D^2}{\hbar^2} \quad (3b)$$

and

$$L_D^2 = \frac{\varepsilon_{Si}^2 k_B T}{q_0^2 n}\frac{\Im_{1/2}(\tilde{\eta}_F)}{\Im_{-1/2}(\tilde{\eta}_F)}. \quad (3c)$$

In Eq. 3, L_D is the screening length for 3D bulk ionized impurities, N_I is the ionized impurity concentration, $\Im_\alpha(\tilde{\eta}_F)$ is the Fermi–Dirac integral of order α, and $\tilde{\eta}_F$ is the reduced Fermi level $\tilde{\eta}_F = (E_F - E_0)/k_B T$. This approach seems to work satisfactorily for doping concentrations up to 10^{18} cm^{-3}.[25] To account for the strong screening at larger carrier concentrations (the structures we consider are doped beyond 10^{19} cm^{-3}), we use the strongly screened transition rate as defined in Ref. 23:

$$\tau(E) = \frac{\hbar}{\pi N_I}\left(\frac{\varepsilon_{Si}}{q_0^2 L_D^2}\right)^2 \frac{1}{N(E)}. \quad (3d)$$

In our model, we merge Eq. 3a and 3d such that Eq. 3a dominates for concentrations below 10^{18} cm^{-3}, and Eq. 3d for concentrations above 10^{19} cm^{-3}. The simple model we use reproduces the *p*-type bulk Si low-field mobility from measurements of Masetti et al. and Jacoboni et al. as shown in Fig. 1.[26–28] At low concentrations, the model gives the expected phonon-limited low-field mobility of $\mu_p = 450\,\text{cm}^2/\text{Vs}$. The phonon-limited scattering MFP is in this case ~7.4 nm. More importantly, our model captures the low-field mobility for carrier concentrations of $p = 10^{19}$ cm^{-3} to 10^{20} cm^{-3}, which are the concentrations in the structures we consider. In this carrier concentration range, the mobility is almost constant and only slightly decreasing as indicated by the measured data and our simulations. The fact that it does not strongly decrease for higher concentrations is a consequence of the stronger screening of the ionized impurities, which weakens scattering and is the reason why very high doping is needed in order to achieve a high conductivity in the grain, and, thus, in the nanocomposite structures (the doping concentration range in the structures we consider is indicated by the red bracket in Fig. 1). The model will refer to *p*-type Si. Thus, *p*-type Si bulk parameters are used, and for the calculation of the DOS we consider all three bands (heavy-hole, light-hole, and split-off) of the electronic structure. Without loss in generality, we keep the electronic structure simple and neglect any effects of strain or lattice deformations that could exist in the two-phase material and could introduce bandstructure modifications. Also, no potential bandstructure modifications due to high doping concentrations will be considered.

Transport Model for the Nanocomposite Material

For the electronic transport calculation in the nanocrystalline material, we adopt the established formalism that describes transport in polycrystalline materials. We assume a sequence of grains of length L_G separated by grain boundary barriers of width L_{GB} as shown in Fig. 2. Transport is limited by the barriers of the grain boundaries and shows thermally activated behavior.[29–31] In the actual calculations, we weight each region with the volume it occupies in the 3D nanocomposite material, e.g., v_G and v_{GB}, for the volume of the grain and grain boundary, respectively, as in Ref. 32 (idealized as cylindrical regions[29]). We then treat the conductivity as the addition of two resistances as:

$$\frac{v_{tot}}{\sigma_{tot}} = \frac{v_G}{\sigma_G} + \frac{v_{GB}}{\sigma_{GB}}, \quad (4)$$

where $v_{tot} = v_G + v_{GB}$, is the total volume of the material. The transport in the network of grains/grain boundaries in the polycrystalline material is here treated within a simplified 1D network of alternating grains and grain boundaries. This is a common approximation in nanocomposites and

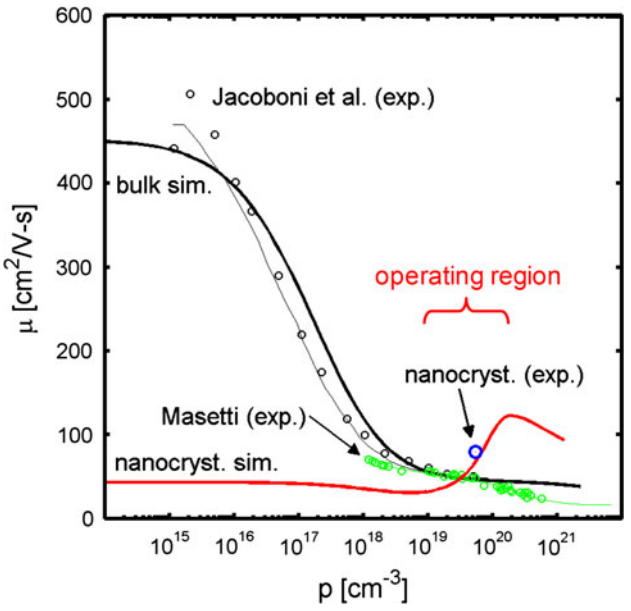

Fig. 1. *p*-type bulk Si mobility measurements from Ref. 26 (*black dots/thin line fitting*), and Ref. 28 (*green dots/thin line fitting*). Simulation results for bulk *p*-type Si are shown in *black*. Simulation results for nanocomposite Si are shown in *solid-red*. Measured mobility in the nanocomposite material is indicated by the *blue dot*. The operating region is indicated at very high doping concentrations, where a region of almost constant (or slightly decreasing) mobility is observed (Color figure online).

polycrystalline materials. Transport in non-uniform materials is typically interpreted by Mott's model of conduction assuming that conduction occurs along a minimum 1D resistance path. Note that, in reality, the transport occurs over a 3D network of grains/grain boundaries, where both series and parallel conduction could co-exist. In addition, using the volume of the regions to scale the conductivity, or even alternatively using their lengths L_G and L_{GB}, is just a simplified approximation. However, as we describe in detail below, we believe that the 1D series model describes our structures better than the parallel conduction model, and that the series connection is the one responsible for the large power factors we experimentally measure and describe in the model.

In the nanocomposite structures we consider, the grain and grain boundary regions are of the order of ~30 and ~2 nm, respectively. For certain scattering mechanisms such as acoustic and optical phonons, for which the MFPs are ~5–10 nm, the grains are not totally diffusive, and in general Eq. 4 is not valid. However, since the transport in the grains is dominated by impurity scattering, with MFPs of the order of a few nanometers (<5 nm), we can safely assume that the carrier momentum is completely relaxed, and transport is diffusive, although the carrier energy is not fully relaxed. The energy spectrum of the conductivity in the grain boundary region is given by:

$$\sigma_{GB}(E) = 0 \quad \text{for} \quad E \le V_b, \tag{5a}$$

$$\sigma_{GB}(E) = \sigma^0_{GB}(E) \quad \text{for} \quad E > V_b. \tag{5b}$$

The model assumes that the grain boundary introduces a barrier, and transport is thermionic over that barrier. Any effects occurring at the interface, or details of the boride phase that forms, could be lumped into the value of σ^0_{GB}, and effectively included as an additional series resistance. In this work, however, we assumed that $\sigma^0_{GB}(E) = \sigma^0_G(E)$.

Once the conductivity of the nanocomposite material is calculated, the mobility can be extracted. This is shown in Fig. 1 (red line). An interesting observation is that the calculated mobility of nanocomposites overpasses the mobility of the uniform material at concentrations above 5×10^{19} cm^{-3}. The reasons for this will be discussed below. Superior transport properties can therefore be achieved in the nanocomposite material at very high doping concentrations.

The Seebeck coefficient is determined by the combined in-series transport in the grains and in the grain boundaries of the nanocrystalline material. There are two regimes of transport as described in Ref. 33 and recently in Ref. 34: (1) when carriers flow *ballistically* (with negligible energy relaxation) in the grain until they reach the grain boundary, and (2) when carrier transport in the grains is *diffusive* (carrier energy is totally relaxed). Note that we use the term *ballistic* referring to the relaxation of the carrier *energy*, although the carrier *momentum* may be fully relaxed due to the very strong ionized impurity scattering. In the first case, the overall Seebeck coefficient is determined by the Seebeck coefficient of the highest barrier, which is the barrier introduced by the grain boundaries.

$$S_{ball} = S_{GB}. \tag{6a}$$

In the second case, when the energy of the carriers is fully relaxed in the grain and grain boundary, the Seebeck coefficient is determined by the weighted average of the Seebeck coefficients of the two regions, with the weighting factor being the temperature drop in each region, which is determined by their thermal conductivities:[32,34]

$$S_{diff} = \frac{S_G \Delta T_G + S_{GB} \Delta T_{GB}}{\Delta T_G + \Delta T_{GB}} = \frac{S_G v_G/\kappa_G + S_{GB} v_{GB}/\kappa_{GB}}{v_G/\kappa_G + v_{GB}/\kappa_{GB}}. \tag{6b}$$

In the case where transport in the grain is neither fully ballistic, nor fully diffusive, we approximate the Seebeck coefficient in the grain by weighting the Seebeck coefficient under (1) the fully ballistic and (2) the fully diffusive cases described by Eqs. 6a and 6b, respectively. The weighting factor is the fraction of energy relaxation in the grain, determined by the MFP of the energy relaxing processes (λ_E), here optical phonons.[33–35] As in the case of estimating the ballisticity of transistor channels, this is given by $C = \lambda_E/(\lambda_E + L_G)$.[35] We mention that at this stage we only consider optical phonons as the energy relaxation mechanism, although carrier–carrier scattering is also an energy relaxation mechanism which could be significant at such high carrier concentrations and will be a subject of a subsequent study. For the grains considered here with lengths $L_G \sim 30$ nm, C is computed to be $C \sim 0.5$. The overall Seebeck coefficient in the grain is then given by:

$$S_G = C S_{GB} + (1 - C) S_{diff}. \tag{6c}$$

Thermal Conductivity Model

The calculation of the Seebeck coefficient (Eq. 6b) has the thermal conductivities of the grain and the grain boundaries as input parameters. These are design parameters for high Seebeck coefficient. Regions with low thermal conductivity have a stronger weight on determining the Seebeck coefficient. It is therefore beneficial to properly design the two phases of the material such that the one with the

lowest thermal conductivity has also the largest Seebeck coefficient. The ratio of the thermal conductivities of the two phases, therefore, is an important design parameter. The phonon thermal conductivity of the grains is calculated using the kinetic theory within the relaxation time approximation. The thermal conductivity along the transport z-direction is given by the following standard expression:[36]

$$\kappa_z = \sum_k \sum_p k_B x^2 \frac{e^x}{V(e^x-1)^2} \upsilon^2(k,p)\tau(k,p)\cos^2[\theta_z(k)] \tag{7}$$

with $x = \hbar\omega(k,p)/k_B T$. In the above equation, k is the phonon wave vector, p is the polarization, υ is the group velocity determined form the slope of the dispersion curves $\upsilon(k,p) = d\omega(k,p)/dk$, ω is the phonon frequency, $\tau(k, p)$ is the phonon relaxation time due to scattering, $\theta_z(k)$ is the angle between the wave vector k and the direction z, and V is the volume of the grain. We used bulk phonon dispersion and relaxation times, assumptions previously validated for Si nanowires and nanofilms.[37] For the phonon scattering relaxation time $\tau(k, p)$ we include phonon–phonon scattering, phonon-defect scattering and phonon-boundary scattering as described in Refs. 37, 38. To calculate the thermal conductivity of the nanocrystalline structure, we assume that the average grain can be represented by a rectangular grain of length L_G and width d. In this work, we assume that the thermal conductivity of the grain boundary κ_{GB} is close to the amorphous limit, in which case the thermal conductivity is set to κ_{GB} = 2 W/mK.

BAND PROFILE FORMATION

The nanocrystalline Si structures we consider consist of grains of average diameter ~30 nm, and grain boundaries of ~2 nm in thickness, which are the geometries of the structures recently realized and described in Refs. 1–5. In those structures, the grain boundaries drastically affect the dopant distribution and the electron and phonon transport. Energy barriers are built up at the grain boundaries due to the crystal and structural inhomogeneities, such as dopant segregation and the creation of a second phase (silicon boride, defects, etc.). Energy selectivity could be provided by these energy barriers and lead to an enhanced Seebeck coefficient. In addition, thermal conductivity reduction and non-uniformity further contribute to the enhancement of ZT. In general, however, improvements in the Seebeck coefficient result in the usual reduction in the electrical conductivity, since the barriers that improve the Seebeck coefficient restrict carrier transport. In this work, however, we show that, when the nanocrystallinity is combined with very high doping, the electrical conductivity can still remain high. The design process is described in Fig. 2, and is as follows. (1) Si nanocrystalline structures are deposited by CVD. The grain sizes are of ~30 nm in diameter and the grain boundaries ~2 nm in thickness. (2) The material is doped with extremely high boron concentrations of 4.4×10^{20} cm^{-3}, which is beyond the solid solubility limit. Figure 2a shows a schematic of the expected initial band diagram in the material. Assuming that all boron dopants remain active, the initial Fermi level $E_{F(i)}$ (dashed red line) resides deep inside (above) the bands (black line), and all states below are occupied with carriers (orange colored region). (3) After sequential annealing steps, boron precipitates, and is then partially deactivated.[39–41] A second silicon-boride phase is formed around the grain boundaries. The final band diagram of the new structure looks like the schematic of Fig. 2b. The formation of the second phase and deactivation of the boron dopants around the grain boundaries increases the barrier heights, introduces depletion regions around the grain boundaries, and reduces the overall electrically active dopant concentration. The new Fermi level $E_{F(f)}$ moves to much lower energy compared to $E_{F(i)}$ (both Fermi levels are shown in Fig. 2a for comparison). Our measurements (and calculations) indicate that the final carrier concentration in the new material as shown in Fig. 2b is $p = 5.6 \times 10^{19}$ cm^{-3}.

The distribution of carriers, however, is possibly highly non-homogeneous. The number of carriers in the middle of the grains is high, can be as high as $p = 1.2 \times 10^{20}$ cm^{-3}, whereas in and around the grain boundaries it can be much lower, or even vanishing small. The value $p = 5.6 \times 10^{19}$ cm^{-3} is, therefore, the average concentration. We note that we do not have access to the actual carrier concentration that could reside in the barrier

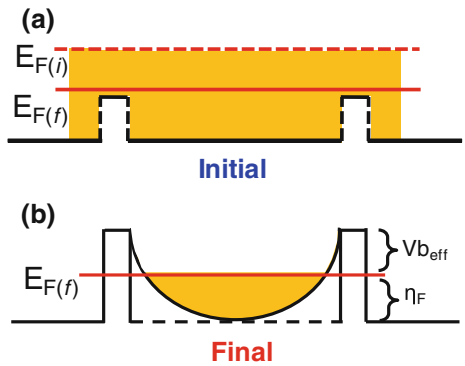

Fig. 2. Schematic of the formation of the nanocomposite material geometry. **a** The nanocrystalline material is highly boron-doped beyond the solid solubility limit. The Fermi level would reside high into the bands (*red-dashed line*). The *orange color* indicates the assumed carrier concentration in the bands of the material. **b** Upon annealing, the boron dopants precipitate, are partially deactivated, and form a second phase around the grain boundaries. The carrier density is further reduced, a depletion region and a potential barrier is formed. The major carrier concentration finally resides in the material in the energy regions specified by the *orange-colored region*. The position of the $E_{F(f)}$ of (**b**) is also indicated in (**a**) to indicate the reduction in the carrier density (Color figure online).

regions. Setting that value to vanishingly small is an assumption. In the simulations, we adjust this number in order to achieve the necessary barrier height that provides the measured Seebeck coefficient. The formation of such band profile as in Fig. 2b allows for very high electrical conductivity in the grain regions, and the still large Seebeck coefficient due to the barriers around the grain boundaries. Finally, an enhanced thermoelectric power factor compared to uniform, homogeneously-doped materials is achieved.

Figure 2 describes in a simplified schematic of how the material structure under consideration is created. The shape of the band profile is very similar to the typical band diagrams for polycrystalline geometries.[29–31] In the structures we consider, however, the precipitation of boron around the grain boundary forms a second-phase, where boron dopant deactivation takes place and higher barriers are built.[39–41] A depletion region is formed around the grain boundaries. Figure 3 shows the simulated band profile after the creation of this depletion region (black line). The blue-dotted lines indicate the actual grain boundary regions. The red-solid line indicates the Fermi level for an average carrier concentration of $p = 5.6 \times 10^{19}$ cm^{-3} that is assumed equal to the concentration measured in our samples. This is much higher than where the Fermi level would have resided if the same carrier concentration had been uniformly distributed in the volume (red-dashed line). As we show later, the high E_F position significantly improves the conductivity of the grains and of the overall structure.

There are two input parameters that we employ in our model in order to capture the experimental measurements (data points shown below in Fig. 5). The first is the amount by which the grain domains are depleted, which determines the position of the Fermi level. The second is the energy barrier height V_B. By setting up these two values, we match the measured electrical conductivity and the Seebeck coefficient at the measured carrier concentration. The barrier height required to achieve the measured Seebeck coefficient is $V_B - E_F \sim 70$ meV. The Fermi level needs to be raised to $E_F - E_0 = 95$ meV to justify the electrical conductivity measured (which corresponds to 45 % grain depletion in our case). Therefore, it is here estimated that $V_B = 165$ meV. Our calculations show that small variations around these numbers would also provide adequate agreement with measurements.

Figure 3b zooms in one of the barriers. We assume that 45 % of the boron dopants in the volume is deactivated, and all deactivation appears in the region around the grain boundaries. That 45 % of the volume (assuming to consist of cylinders as in the inset of Fig. 3b) translates to 3.8 nm of deactivation region around the grain boundary. In order to realize the actual band profile and the actual form of the depletion region that is created, we solve a 1D Poisson equation (in a line that passes through

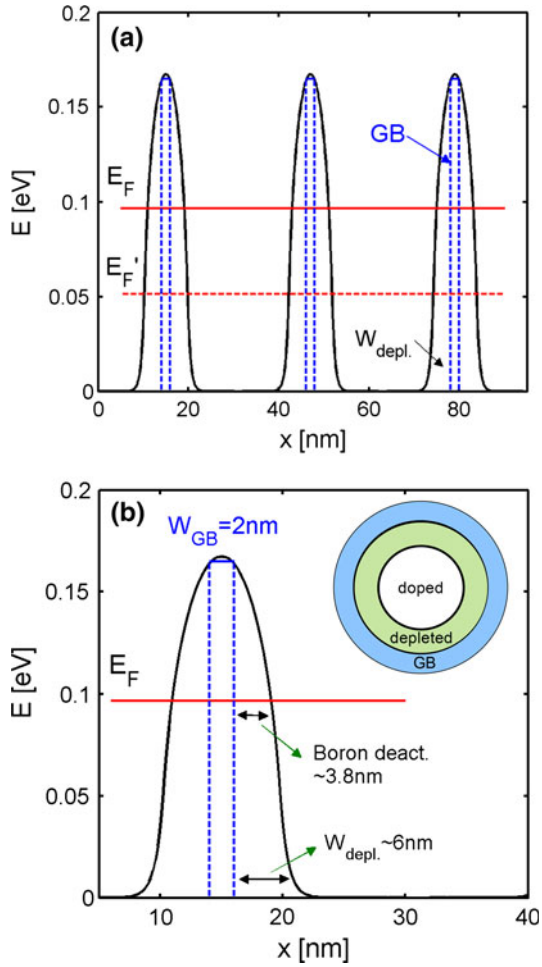

Fig. 3. **a** The nanocrystalline structure, consisting of grains and grain boundaries (*blue-dotted lines*). Depletion regions and potential barriers (*black line*) are formed around the grain boundaries. The position of the Fermi level for average carrier concentrations of 5.6×10^{19} cm^{-3} is indicated for two cases: (1) when the carriers are located only in the grain regions (*solid-red*), and (2) when the carriers can be uniformly distributed in the material (*dashed-red*). **b** Zoom-in of one of the barriers. The depletion region is formed when assuming that 45 % of the boron doping in the volume of the grain is deactivated around the grain boundaries. It results in a 3.8-nm deactivation region around the grain boundaries, and a ~6-nm depletion region. For the depleted volume calculation, we assumed cylindrical grains for symmetry reasons (Color figure online).

the center of the circular grain—taking advantage of the cylindrical symmetry) and obtain the actual depletion region, which in the low energy region extends up to ~6 nm inside the grain. Note that we use cylindrical domains for symmetry reasons, without loss in generality.

THERMOELECTRIC PROPERTIES

The extension of the depletion region, and the available active dopants in the grain, determines the position of the Fermi level. The position of the Fermi level is determined by imposing global charge neutrality in the material. At a certain energy level

E_F, the bandstructure states are occupied according to the Fermi distribution. The amount of charge that resides in the bands is equal to the ionized dopant distribution. The position of the Fermi level determines the MFP of the carriers in the grain, and the conductivity of the grain. This, together with the barrier height with respect to the Fermi level, determines the overall conductivity of the structure. The higher the Fermi level, the higher the conductivity. Figure 4 shows the MFP of carriers in the grain versus energy. The red-dotted line shows the impurity scattering limited MFP, and the red-solid line the total MFP which combines scattering from phonons and ionized impurities. The ionized impurity concentration assumed here is $p = 5.6 \times 10^{19}$ cm^3. At such high doping levels, transport and the carriers MFP for scattering is dominated by ionized impurity scattering. Electron–phonon scattering only has a marginal contribution (see the small deviation of the solid line from the dotted line around the Fermi level). To examine if this is the case in our experimental structures, our measurements show that the resistivity increases monotonically with temperature above 100 K. In a uniform material, this behavior can be observed in two cases: (1) phonon-scattering dominated transport, in which case increase in temperature increases the number of phonons, and (2) impurity-dominated transport under extremely high doping and strong ionized impurity screening conditions, in which case an increase in temperature weakens the screening of ionized impurities by the mobile carriers. In our samples, due to the high doping, impurity scattering dominates over phonon scattering. The dominant scattering mechanism within the grains, however, cannot be directly related to the T-dependence of the overall resistivity of the sample that is the result of a combination of additional mechanisms such as the presence of a network of barriers, also possibly involving thermally activated transport, as well as change in the ionized dopant concentration with temperature. This would require a special analysis within an appropriate and more sophisticated model that is outside the scope of the present work. In the MFPs shown in Fig. 4, around the energies of interest, where the E_F and V_B reside, the impurity-dominated MFP rapidly changes with energy, indicating that the higher the E_F, the higher the conductivity in the grain. In this particular case, changing the position of the Fermi level from E_F' (0.05 eV) to E_F (0.095 eV) as shown in Fig. 3a, increases the carrier MFP by a factor of 3× (see Fig. 4), and accordingly the conductivity in the grain.

The high conductivity in the grain, increases the overall conductivity of the nanocrystalline structure. This is shown in Fig. 5a, which shows the conductivity of the uniformly doped bulk material (black line) and that of the nanocrystalline structure (red line) versus carrier concentration. Two regions can be identified. For carrier concentrations below $p \sim 3 \times 10^{19}$ cm^{-3}, the bulk conductivity is

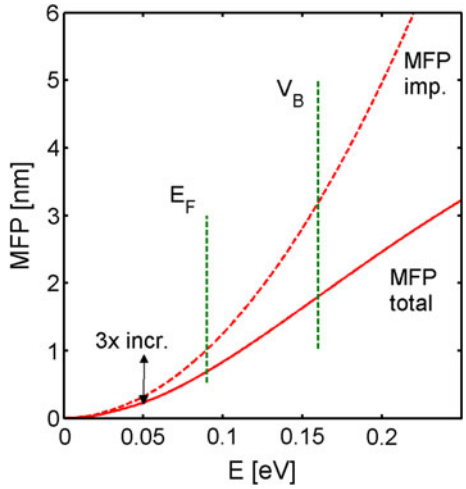

Fig. 4. The mean-free-path for scattering versus energy in the grains of the nanocomposite material. Impurity scattering limited result is shown by the *dashed line*. Total MFP (including phonons) is shown by the *solid line*. The position of the Fermi level at concentrations $p = 5.6 \times 10^{19}$ cm^{-3}, and of the energy barrier are indicated. A 3× increase in the MFP is observed for carriers of energies $E = 50$ meV and $E = 95$ meV.

larger than that of the nanocrystalline structure. At these carrier concentrations, the Fermi level is low, and the barriers significantly reduce the conductivity of the nanocomposite structure. In the second region, for carrier concentrations above $p \sim 3 \times 10^{19}$ cm^{-3}, the conductivity of the nanocomposite structure overpasses that of the uniform bulk structure. The reason is that, for the same carrier concentration, E_F is higher in the composite structure than in the bulk, which increases the carrier MFP and the overall conductivity. This also explains the fact that the mobility of the nanocrystalline material is higher than that of the bulk material at high carrier concentrations, as indicated in Fig. 1. This is shown both in the simulations (red line) and measurements (blue dot for the measured mobility in the nanocrystalline material in Fig. 1). Figure 5b shows the Seebeck coefficient of the composite structure (red line) and that of the uniformly doped bulk material (black line). As expected, the Seebeck coefficient is higher in the case of the composite structure due to the presence of energy filtering barriers. Due to the increase of both the electrical conductivity and the Seebeck coefficient, the power factor in Fig. 5c is much higher for the nanocomposite structure, almost five times higher compared to the uniform bulk material. In Fig. 5a–c, we also indicate the experimental measurements for this structure as in Ref. 5, which are in good agreement with what the model predicts.

Approximations and Assumptions

Transport is treated within a simplified model of a series connection of grain and grain boundaries, rather than assuming conduction within a 3D

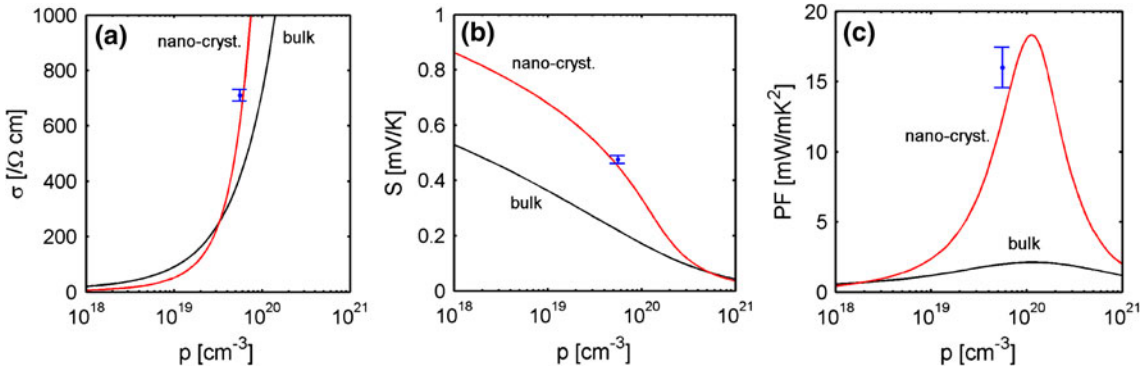

Fig. 5. Simulation results for the thermoelectric coefficients versus carrier concentration for *p*-type bulk Si (*black lines*) and nanocrystalline Si with grain size L_G = 30 nm, grain boundary width L_{GB} = 2 nm, and barrier height V_b = 165 meV (*red lines*). **a** Electrical conductivity, **b** Seebeck coefficient. **c** Power factor. Measurements for the nanocomposite structure with concentrations $p = 5.6 \times 10^{19}$ cm^{-3} are indicated by the blue dots (from Ref. 5) (Color figure online).

nanocrystalline network of the two phases. Our calculations support that an effective series connection results in large power factors as measured and interpreted by the present model. The reason is that the Seebeck coefficient achieved is very high, and is determined by the grain boundaries (barriers), which are the regions of low electrical conductivity. The grain boundaries determine the overall Seebeck coefficient because the energy of the carriers only partially relaxes in the grain regions. In a parallel connection, the situation would instead be the reverse, i.e. the high conductivity region (grain) would determine the overall Seebeck coefficient. In the parallel conduction case, the Seebeck coefficient is given by the weighted average of the Seebeck coefficients in each region with their electrical conductivities as weighting factor:

$$S_{tot} = \frac{S_G\sigma_G + S_{GB}\sigma_{GB}}{\sigma_G + \sigma_{GB}}. \quad (8)$$

In that case, the Seebeck coefficient would have been closer to that of the grain, which is low.

Another approximation is that we neglect any possible bandstructure modifications due to high doping concentrations. Bandstucture modifications would predominantly influence the properties of the grain boundary region and should be taken into account to determine barrier height and profile that are set as parameters in our model. High dopant concentration could also influence the bandstructure of Si within the grains by introducing impurity bands below the band edges. However, our transport formalism is calibrated to the measured mobility data of standard Si. It can, therefore, be considered that such effects have been taken into account implicitly. The use of a different material, or electronic structure, will only change some of the input parameters in our simulations, such as the amount of doping needed to raise the Fermi level high enough, the barrier height, or the depletion region width, but in principle these are design parameters that could be adjusted. The introduction of additional bands by doping should, therefore, not alter the conclusions of this paper.

Our purpose in this work was to point out that, under very high doping concentrations, two-phase materials consisting of series of alternating grains and grain boundaries that introduce potential barriers could provide very high power factors. We provide qualitative and quantitative features for the underlying potential profiles that could result in such an effect. The idea by itself could be possibly useful as a guide to achieving large power factors in polycrystalline materials through simultaneous increase of the Seebeck coefficient and the conductivity. Despite the complexity of nanocrystalline channels of conduction, we believe that, at first order, the effect we describe is the one that takes place in the measurements.

Finally, it was mentioned that the grain boundary barrier height, the overall final carrier concentration, and geometric features such as grain and grain boundary sizes are all input parameters estimated based on the measurements presented in Refs. 1–4. Other than the assumptions and simplifications of the transport formalism, the use of the bulk bandstructure and the treatment of grain boundaries as barriers for carriers, the only fitting parameters used in the model are the active doping concentration in the grain, the percentage of the volume that the depletion region occupies in the grain (which is closely related to the width of the boron deactivation region), and the barrier height. In order to obtain more quantitatively precise features about the boron segregation/precipitation and the extent of the depletion region, one needs to understand the behavior of boron in nanocrystalline Si under high concentrations and temperatures, which is beyond the scope of this work. It could, however, be an important design aspect that would allow further understanding of the mechanisms behind the achievement of high power factors. Note that these generic features and the idea we describe could be

present in a highly doped two-phase system independently of the choice of the banstructure model, or even of the material itself. The use of *p*-type Si is not exclusive to our analysis, as we use it in relation to the nanocrystalline structures experimentally characterized.

SUMMARY AND CONCLUSIONS

We present a simple semiclassical model that describes thermoelectric transport in heavily boron-doped, nanocrystalline, Si materials of grain sizes <100 nm. We consider both electron and phonon transport. The model successfully explains measured data of power factor enhancement in this material, through a *simultaneous* improvement of the electrical conductivity and the Seebeck coefficient for some range of carrier densities. This is attributed to: (1) the precipitation of a silicon-boride phase around the grain boundaries which improves carrier energy filtering, and (2) high boron concentrations in the grains of the nanocrystalline material, which improve the overall electrical conductivity. Our investigation, which is also supported by measurements, points to new directions for power factor improvements in two-phase nanocomposite materials by simultaneously achieving high Seebeck coefficients and high electrical conductivity compared to the bulk uniform material values. The high power factors, together with the thermal conductivity reduction that can be achieved in such nanostructured materials, could potentially lead to large *ZT* figures of merit.

REFERENCES

1. D. Narducci, E. Selezneva, A. Arcari, G.F. Cerofolini, E. Romano, R. Tonini, and G. Ottaviani, *MRS Proceedings*, 1314, mrsf10-1314-ll05-16 (2011). doi:10.1557/opl.2011.511.
2. D. Narducci, E. Selezneva, G.F. Cerofolini, E. Romano, R. Tonini, and G. Ottaviani, *Proceedings of the 8th European Conference on Thermoelectrics* (22–24 September, 2010, Como, Italy), pp. 141–146.
3. D. Narducci, E. Selezneva, G.F. Cerofolini, S. Frabboni, and G. Ottaviani, *J. Solid State Chem.* 193, 19 (2012).
4. D. Narducci, E. Selezneva, G.F. Cerofolini, S. Frabboni, and G. Ottaviani, *AIP Conf. Proc.* 1449, 311 (2012). doi: 10.1063/1.4731559.
5. N. Neophytou, X. Zianni, H. Kosina, S. Frabboni, B. Lorenzi, and D. Narducci, *Nanotechnology* 24, 205402 (2013).
6. R. Venkatasubramanian, E. Siivola, T. Colpitts, and B. O'Quinn, *Nature* 413, 597–602 (2001).
7. L.D. Zhao, S.H. Lo, J.Q. He, L. Hao, K. Biswas, J. Androulakis, C.I. Wu, T.P. Hogan, D.Y. Chung, V.P. Dravid, and M.G. Kanatzidis, *J. Am. Chem. Soc.* 133, 20476–20487 (2011).
8. A.I. Boukai, Y. Bunimovich, J.T. Kheli, J.-K. Yu, W.A.G. III, and J.R. Heath, *Nature* 451, 168–171 (2008).
9. A.I. Hochbaum, R. Chen, R.D. Delgado, W. Liang, E.C. Garnett, M. Najarian, A. Majumdar, and P. Yang, *Nature* 451, 163–168 (2008).
10. J. Tang, H.-T. Wang, D.H. Lee, M. Fardy, Z. Huo, T.P. Russell, and P. Yang, *Nano Lett.* 10, 4279–4283 (2010).
11. K. Nielsch, J. Bachmann, J. Kimling, and H. Boettner, *Adv. Energy Mater.* 1, 713–731 (2011).
12. C.J. Vineis, A. Shakouri, A. Majumdar, and M.C. Kanatzidis, *Adv. Mater.* 22, 3970–3980 (2010).
13. F. Song, L. Wu, and S. Liang, *Nanotechnology* 23, 085401 (2012).
14. Y. Yang, D.K. Taggart, M.H. Cheng, J.C. Hemminger, and R.M. Penner, *J. Phys. Chem. Lett.* 1, 3004–3011 (2010).
15. W. Xu, Y. Shi, and H. Hadim, *Nanotechnology* 21, 395303 (2010).
16. H. Ohta, et al., *Nat. Mater.* 6, 129–134 (2007).
17. H. Ikeda and F. Salleh, *Appl. Phys. Lett.* 96, 012106 (2010).
18. C.M. Jaworski, V. Kulbachinskii, and J.P. Heremans, *Phys. Rev. B* 80, 125208 (2009).
19. D. Vashaee and A. Shakouri, *Phys. Rev. Lett.* 92, 106103 (2004).
20. N. Neophytou and H. Kosina, *Phys. Rev. B* 83, 245305 (2011).
21. T.J. Scheidemantel, C.A. Draxl, T. Thonhauser, J.V. Badding, and J.O. Sofo, *Phys. Rev. B* 68, 125210 (2003).
22. R. Kim, S. Datta, and M.S. Lundstrom, *J. Appl. Phys.* 105, 034506 (2009).
23. M. Lundstrom, *Fundamentals of Carrier Transport* (Cambridge: Cambridge University Press, 2000).
24. H. Kosina and G.K. Grujin, *Solid State Electron.* 42, 331–338 (1998).
25. A.T. Ramu, L.E. Cassels, N.H. Hackman, H. Lu, J.M.O. Zide, and J.E. Bowels, *J. Appl. Phys.* 107, 083707 (2010).
26. C. Jacoboni and L. Reggiani, *Rev. Mod. Phys.* 55, 645 (1983).
27. Ioffe Physiotechnical Institute, *Physical Properties of Semiconductors* (St. Petersburg, Russia: Russian Federation, 1998–2001), http://www.ioffe.ru/SVA/.
28. G. Masetti, M. Severi, and S. Solmi, *IEEE Trans. Electr. Dev.* 30, 764 (1983).
29. J.W. Orton and M.J. Powell, *Rep. Prog. Phys.* 43, 1263 (1980).
30. J.Y.W. Seto, *J. Appl. Phys.* 46, 5247 (1975).
31. F.V. Farmakis, J. Brini, G. Kamarinos, C.T. Angelis, C.A. Dimitriadis, and M. Miyasaka, *IEEE Trans. Electr. Dev.* 48, 701 (2001).
32. M. Zebarjadi, G. Joshi, G. Zhu, B. Yu, A. Minnich, Y. Lan, X. Wang, M. Dresselhaus, Z. Ren, and G. Chen, *Nano Lett.* 11, 2225–2230 (2011).
33. Y. Nishio and T. Hirano, *Jpn. J. Appl. Phys.* 36, 170–174 (1997).
34. R. Kim and M. Lundstrom, *J. Appl. Phys.* 110, 034511 (2011).
35. M. Lundstrom, *Electr. Dev. Lett.* 22, 293–295 (2001).
36. J.M. Ziman, *Electrons and Phonons* (Cambridge: Cambridge University Press, 2001).
37. P. Chantrenne, J.L. Barrat, X. Blase, and J.D. Gale, *J. Appl. Phys.* 97, 104318 (2005).
38. M.G. Holland, *Phys. Rev.* 134, A471 (1964).
39. S. Duguay, A. Colin, D. Mathiot, P. Morin, and D. Blavette, *J. Appl. Phys.* 108, 034911 (2010).
40. S. Duguay, T. Philippe, F. Cristiano, and D. Blavette, *Appl. Phys. Lett.* 97, 242104 (2010).
41. O.C. Miredin, F. Cristiano, P.-F. Fazzini, D. Mangelinck, and D. Blavette, *Thin Solid Films* 534, 62–65 (2013).